PCCP

Accepted Manuscript

ROYAL SOCIETY OF CHEMISTRY

www.rsc.org/pccp

Journal Name

ARTICLE

The (0001) Surfaces of α-Fe_2O_3 Nanocrystals are Preferentially Activated for Water Oxidation by Ni Doping

Received 00th January 20xx,
Accepted 00th January 20xx

DOI: 10.1039/x0xx00000x

www.rsc.org/

Peng Zhao,[a] Fan Wu,[b] Coleman X. Kronawitter,[a] Zhu Chen,[a] Nan Yao[b] and Bruce E. Koel*[a]

Photoelectrochemical water oxidation on hematite has been extensively studied, yet the relationship between the various facets exposed, heteroatom doping, and associated electrocatalytic activity has not been adequately explored. Here, hematite nanocrystals were synthesized with continuous tuning of the aspect-ratio and fine control of the surface area ratio of the (0001) facet with respect to other surfaces. The samples were doped with nickel, which was confirmed using the combined results of HRTEM, SEM, XRD, Raman, BET, and XPS measurements. The surface area ratio of the hexagonal (0001) surface with respect to all surfaces was tuned from 98% to 30%. Ni doping was accomplished by diffusion of Ni clusters into the subsurface region, which forms a uniformly doped $Ni_xFe_{2-x}O_3$ surface overlayer that improves the electrocatalytic activity of water oxidation. These results are discussed in the context of a theoretical prediction and subsequent surface science validation that Ni doping facilitates the water oxidation reaction on hematite (0001) surfaces. Electrochemical testing of water oxidation catalysis was carried out on doped and shape-controlled hematite nanocrystals. The enhancement of water oxidation activity by Ni-doping increased as the surface area ratio of the (0001) facet of hematite nanocrystals increased, consistent with the theoretical predictions and surface science studies.

Introduction

Hematite (α-Fe_2O_3) has been intensely investigated as a constituent material for photoelectrodes enabling the oxygen evolution reaction (OER), a key half-reaction required in solar fuel production schemes. It has an optimal band gap (2.1–2.2 eV) and is abundant, nontoxic, and chemically stable in aqueous nonacidic electrolytes.[1-5] However, α-Fe_2O_3 photoelectrodes are impeded by several shortcomings, including perhaps most importantly their low associated catalytic efficiency for the OER. This is currently responsible for much of the overall efficiency loss associated with solar-driven hydrogen generation by water splitting using hematite photoelectrodes. To address this issue, researchers have actively pursued surface modification with cocatalysts,[6, 7] composite oxides,[8-10] or heteroatom doping[11-14] as a means to improve reaction kinetics and reduce overpotentials.

Recently, Carter and co-workers[15] by performing periodic density functional theory + U calculations proposed a detailed water oxidation mechanism on α-Fe_2O_3(0001) surfaces. On the basis of their proposed mechanism, and after consideration of several substitutional surface dopants, they predicted that a Ni-doped α-Fe_2O_3(0001) surface yields the most thermodynamically favored reaction pathway. In fundamental studies using well-defined hematite film surfaces on a single crystal substrate, we recently obtained experimental support for this prediction by using a combination of surface science and electrochemistry experiments to control the Ni dopant concentration at the surface, characterize reactive species at the (0001) surface stabilized at low temperatures, and evaluate the electrochemical performance of these materials for water oxidation.[16] What is now needed is to apply the insights from these studies toward the design of electrodes that can be fabricated by scalable techniques. Herein, we report on the use of solution synthesis techniques to fabricate electrodes with controlled surface composition and crystal facet exposure. These results demonstrate scalable nanomaterial production and provide additional experimental validation of the theory and surface science model studies.

Many studies have reported the controlled growth[17-20] and nanostructure-related properties[21-26] of functional nanocrystals. Wu and co-workers have studied (0001)-facet-tuning of hematite nanocrystals[19] and their application in lithium-ion batteries.[21] No studies have been reported that investigate the effects of Ni-doping on hematite nanocrystals with controlled facet exposure and the application of these materials for water oxidation catalysis.

In this article, we compare the morphology, crystal structure, chemical composition, and electrochemical properties of hematite and Ni-doped hematite nanomaterials with different relative concentrations of exposed (0001) surfaces. Specifically the influence of these characteristics on

---

[a] Department of Chemical and Biological Engineering, Princeton University, Princeton, NJ 08544, USA.

[b] Princeton Institute for Science and Technology of Materials, Princeton University, Princeton, NJ 08544, USA.

† Footnotes relating to the title and/or authors should appear here.

Electronic Supplementary Information (ESI) available: [details of any supplementary information available should be included here]. See DOI: 10.1039/x0xx00000x activity for electrocatalytic water oxidation is presented. The samples were tested by cyclic voltammetry (CV) in an electrochemical cell, where we found that the enhancement of water oxidation activity by Ni-doping increases as the surface area ratio of the (0001) facet increases with respect to other surfaces of hematite nanocrystals.

Experimental

The synthesis procedure of α-Fe_2O_3 nanoplates used is a modification of a hydrothermal method reported previously.[19] First, 0.113 g of $FeCl_3$ (0.7 mmol, Sigma Aldrich) was dissolved under magnetic stirring in ethanol with various amount of de-ionized (DI) water (0, 0.2, 0.5, 0.8, and 1.5 mL labeled as Hem-1 to Hem-5, respectively). The total volume of ethanol and water was kept at 7 mL. After stirring for 10 minutes, 0.56 g of sodium acetate (CH_3COONa, Fisher) was added while stirring. The mixture was sealed in a Teflon-lined stainless steel autoclave (10 mL) at 180 °C for 12 h. The precipitates were washed with DI water and ethanol several times, and then dried at 60 °C for 1 h.

The Hem-x-Ni-1 (x = 1, 2, 3, 4, 5) samples, where the Ni index will be used to indicate different levels of doping, were prepared in two steps. First, 16 mg of as-synthesized α-Fe_2O_3 nanoplates and 1.5 mg of $Ni(NO_3)_2{\cdot}6H_2O$ (0.005 mmol, Sigma Aldrich) were dispersed in 9.925 mL ethanol by sonication for 20 min and stirring for 1 h, to which an aqueous solution (0.075 mL) of NaOH (2 mg, 0.05 mmol) and $NaBH_4$ (0.5 mg, 0.013 mmol) was then slowly added. Other Hem-x-Ni-y (y=2, 3) were also prepared by following the same process, but using: 3 mg of $Ni(NO_3)_2{\cdot}6H_2O$ (0.01 mmol), 0.15 mL aqueous solution of NaOH (4 mg, 0.1 mmol) and $NaBH_4$ (1 mg, 0.026 mmol) for Hem-x-Ni-2; and 6 mg of $Ni(NO_3)_2{\cdot}6H_2O$ (0.02 mmol), 0.3 mL aqueous solution of NaOH (8 mg, 0.2 mmol) and $NaBH_4$ (2 mg, 0.053 mmol) for Hem-x-Ni-3. The obtained products were centrifuged and dried in vacuum immediately. After that, the samples were annealed in a N_2 flow at 700 K for 2 h.

A Philips CM200 FEG-Transmission electron microscope (TEM) equipped with a Gatan 678 Imaging Filter operating at 200 keV was used to acquire high-resolution TEM images. To prepare the samples for TEM analysis, the hematite samples were dispersed in ethanol and then deposited onto 300 mesh holey carbon-coated Cu grids. A scanning electron microscope (SEM) equipped with a field-emission gun (FE-SEM Quanta 400 FEG, FEI) was used to image the morphology and mesoscale structure of the nanocrystals. X-ray powder diffraction (XRD) patterns were acquired with a Rigaku MiniFlex X-Ray Diffractometer using Cu Kα radiation. Raman spectroscopy was undertaken using a HORIBA (with 632.8 nm He-Ne laser) Raman spectrophotometer. The surface area was determined from nitrogen adsorption data (Gemini V, Micrometrics Instruments Corporation) by Brunauer, Emmett, and Teller (BET) method.[27] The high resolution X-ray photoelectron spectroscopy (HR-XPS) experiments, carried out in an UHV system with a base pressure of 2.0×10^{-10} Torr, were performed using a VG Scienta MX 650 monochromated X-ray source (Al Kα, 450 W, 15 kV) and a VG Scienta R3000 analyzer equipped with a multi-channel detector system.

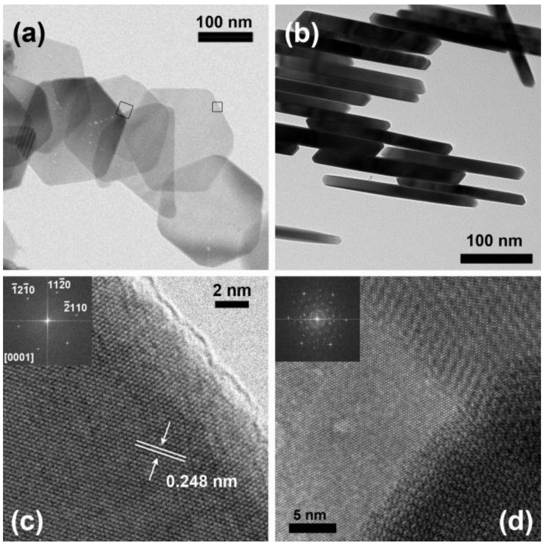

Fig. 1 (a, b) TEM images of several horizontally and vertically lying nanoplates. (c, d) HRTEM images and their related FFT patterns (inset) from the black squares in Fig. 1a, where (c) is from the smaller black square on the right and (d) is from the larger black square on the left.

Electrochemical evaluation was performed using rotating disc electrode voltammetry (RDE). α-Fe_2O_3 nanocrystals were dispersed in a 50%-50% volume mixture of de-ionized water and ethanol containing 0.2 wt% of Nafion® solution (LIQUION® LQ-1115). After sonication, the working electrode was prepared by depositing various amounts of catalyst solution onto a glassy carbon electrode (PINE Research Instrument, 5 mm diameter) to achieve a loading of catalysts with a total surface area of 0.01 m^2, based on BET analysis. The working electrode along with a platinum wire counter electrode and a double-junction Ag/AgCl reference electrode were immersed in 0.1 M KOH electrolyte to perform cyclic voltammetry (CV) at a scan rate of 10 $mV{\cdot}s^{-1}$.

Results and discussion

α-Fe_2O_3 Nanoplates with (0001) facets exposed

The morphologies and crystal structures of the hematite nanoplates were investigated using TEM. Fig. 1a and b show TEM images in which well-crystallized hexagonal nanoplates with a width of around 200 nm and a thickness of around 15 nm are observed. The aspect ratio (thickness/width) is about 0.08. To identify the exposed facets, HRTEM and fast Fourier transformation (FFT) were performed. As shown in Fig. 1c, which is a magnified region labeled by the smaller black square in Fig. 1a, the nanoplate is a single crystal with a lattice spacing of 0.248 nm. This spacing corresponds to hematite {1 1 -2 0} planes. The inset FFT pattern shows six equivalent {1 1 -2 0} diffraction spots, suggesting that the top and bottom surfaces can be ascribed to the (0001) basal plane. Fig. 1d displays several nanoplates stacked together. With lattices in different rotational positions, the particles possess a long-range superstructure, which is consistent with the inset FFT pattern.

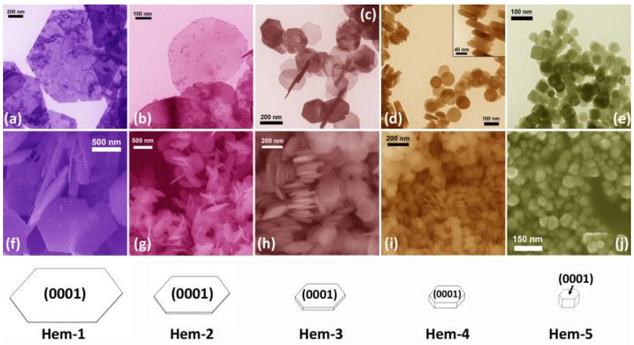

Fig. 2 TEM (top row) and SEM (bottom row) images of hematite samples grown from the solvent with an addition of water of (a, f) 0 mL (Hem-1), (b, g) 0.2 mL (Hem-2), (c, h) 0.5 mL (Hem-3), (d, i) 0.8 mL (Hem-4), and (e, j) 1.5 mL (Hem-5). The total volume of solvent was kept at 7.0 mL and the solvent contained 0.56 g sodium acetate. Schematic representations (not to scale) tracking the changes in the size and morphology of the hematite nanocrystals by addition of water are provided below the corresponding images.

The presence of water plays a significant role in the growth of these hematite nanoplates, which has been reported before.[19] Fig. 2 shows that the hematite crystal shapes have a sequential variation from large nanosheets and nanoplates and to nanograins with an increased aspect ratio. With the addition of water in the reaction volume from 0 to 1.5 mL, the diameters of the nanocrystals (labeled as Hem-1 to Hem-5) decrease from 1000 to 500, 200, 100, and 60 nm and the thicknesses increase from 10 to 15, 20, 30, and 60 nm. In all cases the particles have a narrow size distribution. Across the series the aspect ratio changes 100x, from 0.01 to 1.0. The surface area ratio of the hexagonal (0001) surface with respect to all surfaces becomes smaller, decreasing from 98% to 30%.

In Fig. 3a, XRD patterns, which all match well with PDF#33-0664 for rhombohedral α-Fe_2O_3, confirm that all products are hematite. An increase of the intensities of the 1120 peak at 32.8° and a decrease of that of the 1014 peak at 35.2° are observed, implying a decrease of particle width and increase of thickness. The Raman spectra of hematite samples were measured, and it was observed that there are two A_{1g} modes corresponding to bands at 222 and 499 cm^{-1}, and four E_g modes corresponding to bands at 242, 288, 412 and 610 cm^{-1} (Fig. 3b). As the particle size is decreased, the A_{1g} mode at 222 cm^{-1} significantly increases and the E_g mode at 412 cm^{-1} decreases, which is consistent with prior reports.[19] To determine the surface area, BET analysis (Fig. 3c) was performed on samples with different shape and size by investigating N_2 adsorption-desorption isotherms (Fig. S1). Based on the assumption that these samples are hexagonal nanoplates with diameters of 1000, 500, 200, 100 and 60 nm and thicknesses of 10, 15, 20, 30 and 60 nm, respectively, the specific surface areas were calculated to be 38.6, 25.7, 23.2, 21.3 and 20.8 $m^2 \cdot g^{-1}$. The experimental BET specific surface areas were 42.2, 27.1, 24.2, 21.2 and 20.2 $m^2 \cdot g^{-1}$, respectively, which are very close to the calculated results. This indicates that the surface area and ratios of the (0001) surfaces of the prepared materials are consistent with the changes in size and morphology of the hematite nanocrystals rendered schematically in Fig. 2. By employing the same method of depositing these nanoparticles, we expect that the surface area and ratios of (0001) surfaces of the electrodes prepared for electrochemical measurements would be close to those from the BET analysis results. In summary, the results from XRD, Raman, and BET indicate that by changing the conditions of synthesis we could continuously tune the shapes, sizes, and surface area ratios of (0001) facets with respect to all surfaces of nanocrystals (from 98% to 30%), while maintaining the hematite phase.

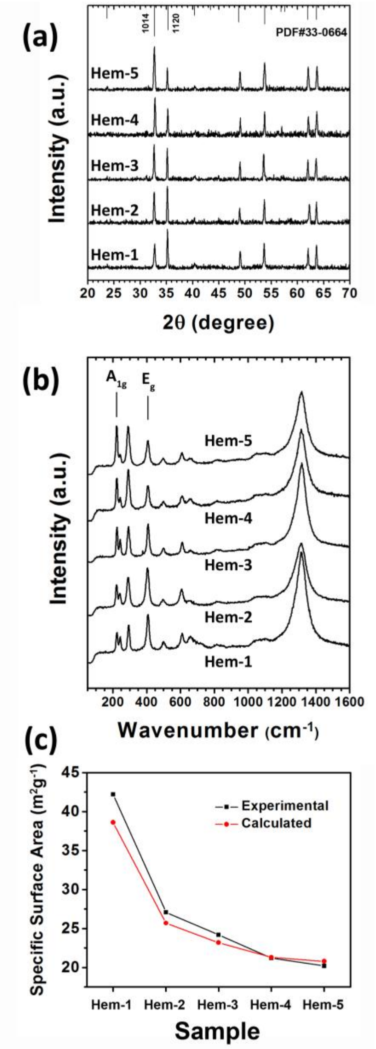

Fig. 3 (A) XRD patterns of samples Hem-1 to Hem-5. The bars are from PDF#33-0664 for rhombohedral α-Fe_2O_3. (B) Raman spectra of samples Hem-1 to Hem-5. (C) BET specific surface area (black squares) of samples Hem-1 to Hem-5, and approximate calculation of specific surface area (red circles).

Doping of Ni into α-Fe_2O_3 nanoplates

To synthesize the Ni-modified samples, we deposited Ni particles on the hematite nanoplates. Addition of aqueous NaOH and $NaBH_4$ to an ethanol solution of α-Fe_2O_3 nanoplates and different concentrations of $Ni(NO_3)_2$ led to the formation of different quantities of Ni nanoparticles on the nanoplate surfaces. We then heated the products in N_2 for 2 h. In this study, we found that post-deposition annealing temperature strongly affects the electrocatalytic activity of Ni-doped α-Fe_2O_3. We observed an increase in the current density when the annealing temperature was increased from 500 to 700 K, while a noticeable decrease occurred when the temperature was increased from 700 to 800 K on all samples (Figure S6). This may be attributed to that, at lower temperature, Ni cannot be doped into the surface, while at higher temperature, the nanocrystals will agglomerate or Ni from the surface is diffused into the bulk, and the sample exhibits worse performance. The current density reached the highest value when samples were annealed to 700 K, and so these conditions were chosen for discussion of Ni-doping and electrochemical characterization in this paper. Structural analysis of the modified samples shows the incorporation of Ni into the α-Fe_2O_3 nanoplates. Fig. 4a and b show TEM images of hematite samples with the deposited Ni nanoparticles before annealing. Ni clusters with diameter less than 5 nm were observed at similar concentration on both hexagonal planes and edges, while the morphology of the nanoplates did not change. This indicates that the different surfaces of the prepared materials have similar amounts of Ni deposited, which should lead to similar doping concentrations after annealing. In the samples after annealing, small Ni clusters were no longer observed, which suggests they either diffused into the nanoplates or detached from the nanoplates. In addition, the edges of the nanoplates tended to be round compared to the flat edges observed before annealing. The diameter and thickness of all samples did not change after doping, which suggests the surface area ratio of (0001) facets did not change after doping.

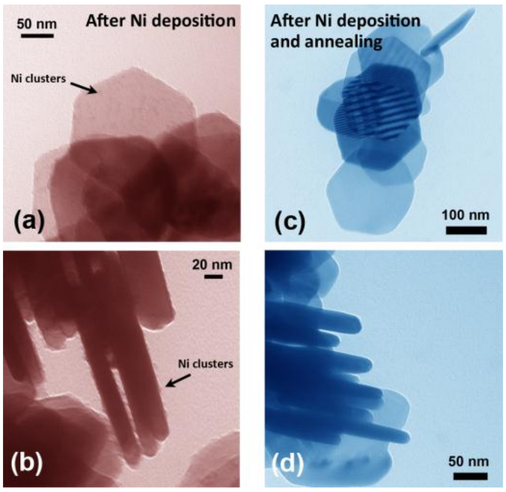

Fig. 4 TEM images of Hem-3 hematite samples (a, b) deposited with Ni, and then (c, d) heated to 700 K in N_2 for 2 h (labeled as Hem-3-Ni-3).

To confirm that Ni exists in the nanoplate samples after annealing, XPS was performed (Fig. 5). Ni 2p XPS spectra in Fig. 5a show that the nanoparticles obtained from reducing $Ni(NO_3)_2$ by $NaBH_4$ consisted mostly of Ni(0) with a small amount of Ni(II). While Ni deposition forms mostly metallic Ni(0), likely in clusters, after heating to 700 K in N_2 there is no Ni(0) peak and only a Ni(II) peak with a Ni(III) shoulder (Fig. 5b). These data indicate that the Ni clusters diffused into the hematite surface and exist there as Ni(II). Ni concentrations of all samples after doping were determined by XPS and expressed as the Ni/(Ni+Fe)% atomic ratio, as summarized in Table S1.

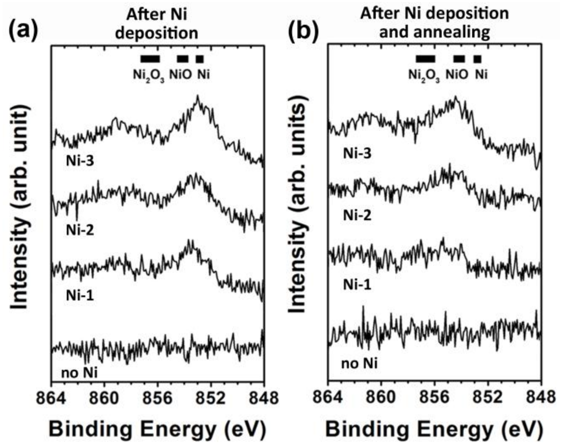

Fig. 5 Ni 2p XPS spectra of (a) clean and Ni-deposited Hem-3 samples before annealing, and (b) clean and Ni(II)-doped Hem-3 samples obtained after heating to 700 K in N_2.

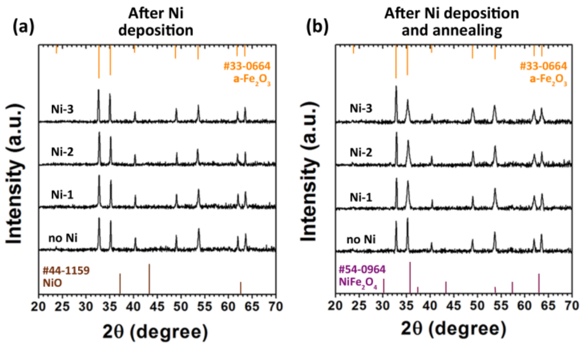

Fig. 6 XRD patterns of (a) clean and Ni-deposited Hem-3 samples before annealing, and (b) clean and Ni-doped Hem-3 samples, obtained after heating to 700 K in N_2 for 2 h. Bars are shown in these figures from PDF#33-0664 for rhombohedral α-Fe_2O_3 (orange at top), PDF#44-1159 for nickel oxide NiO (brown at bottom left), and PDF#54-0964 for nickel ferrite $NiFe_2O_4$ (purple at bottom right).

We carried out XRD analysis to assess the crystal structures of Ni-modified hematite samples, as shown in Fig. 6. All XRD peaks could be indexed to the characteristic peaks of hematite, and no peaks corresponding to nickel, nickel oxide or nickel ferrite were observed for Ni-deposited or Ni-doped samples, suggesting that the Ni incorporation was not associated with any new long-range order in the crystals. The only change from annealing and Ni incorporation compared to the undoped samples is an increase in the full-width-at-half-maximum (fwhm), implying a more disordered α-Fe_2O_3 lattice.

All these results suggest that Ni atoms are substitutionally doped into the hematite lattice, but is not conclusive by itself. Raman spectroscopy was used to further examine the phase of the films, as shown in Fig. 7. Raman spectra of un-annealed hematite samples with deposited Ni clusters were similar to the Raman spectra of clean hematite samples. This is supportive evidence that Ni is deposited as Ni(0) clusters, since

Raman is very sensitive to metal-oxygen bonds, including Ni-O bonds. Additionally, for the samples after annealing, the peaks located at ~660 cm^{-1} were more intense as we increased the Ni concentration during the deposition. This peak has been reported to be associated with the disorder-induced activation of the IR-active mode present at the same wavenumber.[28] The presence of other metal ions replacing iron may explain the appearance in the Raman spectra of that vibrational mode. A similar disordered phase has been detected by Raman spectroscopy performed on doped α-Fe_2O_3 films in previous studies.[11, 14] We also carried out XRD and Raman measurements on samples with different sizes and shapes (Hem-1 to Hem-5), and the results were similar to those of sample Hem-3 shown in Figures 6 and 7. Also XPS analysis was performed on samples Hem-1 to Hem-5, and while the Ni concentration varied, as shown in Table S1, all of the spectra indicated the same Ni oxidation states. All of these data showed that on samples with different sizes and shapes, higher Ni concentration leads to similar surface structure.

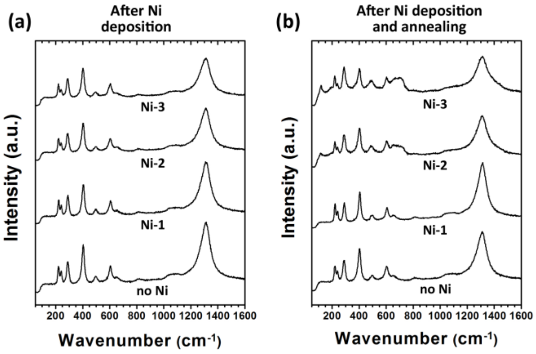

Fig. 7 Raman spectra of (a) clean and Ni-deposited Hem-3 samples before annealing, and (b) clean and Ni-doped Hem-3 samples obtained after heating to 700 K in N_2.

To further probe the structure of these Ni-doped hematite samples, HRTEM analysis was performed (Fig. 8a). A ~6 nm thick layer near the surface had darker contrast than that of bulk hematite, indicating a uniform doping of Ni atoms into hematite. The contrast difference between the surface layer and the bulk originates from the variation between atomic weights of Ni and Fe. A careful analysis of the HRTEM image reveals that a uniform atomic arrangement along the {1 0 -1 4} face exists from the surface all the way to the inside or bulk of the nanoplates, indicating that the doped Ni atoms most likely occupy the lattice positions of Fe atoms rather than occupying interstitial positions, a scenario which would yield sequential interruptions in the lattice arrangement. As a result the lattice of pristine hematite is well preserved after Ni incorporation, with no obvious adhered particles. The situation here is similar to, but distinct from, a previously reported case[29] in which the doped layer was disordered. To confirm a Fe_2O_3-like local structure for the thin $Ni_xFe_{2-x}O_3$ surface overlayer and of the pristine hematite, Fast Fourier Transformation (FFT) analyses were performed on both the surface layer and the bulk region, as shown in Fig. 8b and c. Both of them can be uniquely and unequivocally indexed to the [-1 2 -1 0] zone axis of α-Fe_2O_3, indicating that the crystal lattice of α-Fe_2O_3 is well preserved. However, the Fe_2O_3-like local structure of the thin $Ni_xFe_{2-x}O_3$ surface overlayer is slightly influenced by the incorporation of Ni atoms, as manifested by the distortion/movement of the {1 0 -1 4} diffraction points. For the surface layer, the {1 0 -1 4} diffraction points are closer to the central bright spot in reciprocal space, indicating a larger {1 0 -1 4} interplanar distance of the $Ni_xFe_{2-x}O_3$ surface overlayer than that of α-Fe_2O_3 in real space. The structure of the thin $Ni_xFe_{2-x}O_3$ surface overlayer with increased disorder is therefore consistent with the structures investigated previously by theory[15] and subsequently by surface science measurements.[16] Additional STEM characterization would provide more information on the dopant distribution, which is planned.

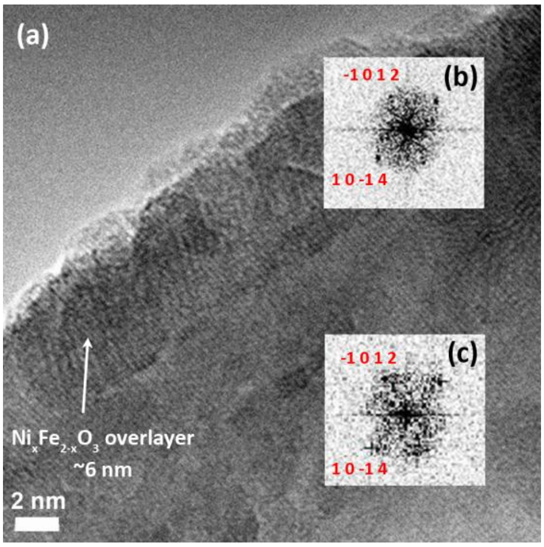

Fig. 8 (a) Typical HRTEM image of doped hematite nanoplates showing the thin $Ni_xFe_{2-x}O_3$ surface overlayer and the α-Fe_2O_3 bulk from top-view. (b, c) Fast Fourier Transformation (FFT) of (b) the thin $Ni_xFe_{2-x}O_3$ surface overlayer and (c) α-Fe_2O_3 bulk.

Oxygen evolution reaction by different shapes of un-doped and doped hematite

Surfaces of catalysts play an important role in the formation of active sites, the adsorption of water molecules, and the execution of oxidative steps for the oxygen evolution reaction. The different chemical environments of the different hematite facets after doping should lead to different electrocatalytic activity. As mentioned above, for differing shapes of doped hematite, the surface area ratios of (0001) facets with respect to other surfaces were significantly different, ranging from 98% to 30%. Water oxidation activities of the Ni-doped α-Fe_2O_3 samples were compared to those of the undoped samples in 0.1 M KOH solution by cyclic voltammetry. The electrocatalytic activity of each shape was measured in order to determine the influence of the amount of exposed (0001) facets, and furthermore the electrocatalytic activity enhancement from doping of each shape was measured in order to determine the separate influence of Ni doping.

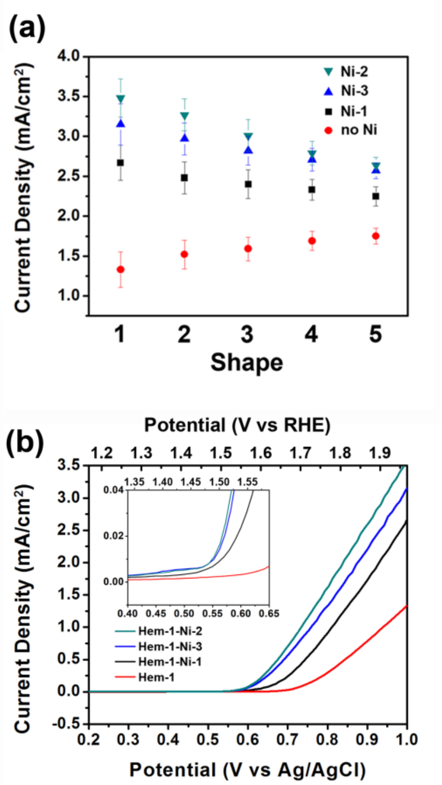

Fig. 9 (a) Trends in electrochemical performance at 1.0 $V_{Ag/AgCl}$ for hematite samples before doping and after different levels of Ni doping for the oxygen evolution reaction are shown for different sizes and shapes. Shapes 1 to 5 denote samples Hem-1 to Hem-5. The amounts of samples loaded were calculated by BET specific surface area to ensure that samples with different shapes had same total surface area. All experiments were taken three times to ensure reproducibility. Values of the current density at 1.0 $V_{Ag/AgCl}$ for the different samples are given in Table S2. (b) Current-potential plots in the dark for Hem-1 samples without Ni and with different levels of doping obtained by Ni deposition followed with heating to 700 K in N_2 for 2 h. These measurements were made in 0.1 M KOH with a sweep rate of 10 mV/s. The insets show magnification of the regions where the onset potential occurs. Only anodic scans are shown here.

Fig. 9b shows current density-potential curves for α-Fe_2O_3 nanoplates with 1000 nm diameter and 10 nm thickness (Hem-1) before doping, and then after different levels of doping. After doping of 9.2% Ni of the sample Hem-1-Ni-1, an enhancement in the current for water oxidation was observed, reaching 2.7 mA/cm^2 at a potential of 1.0 $V_{Ag/AgCl}$, compared with 1.3 mA/cm^2 for the Ni-free hematite sample. In the enlarged onset region where the current starts to rise (Fig. 9b inset), the onset of water oxidation shifts to lower potential as the sample was doped with higher concentration of Ni. However, the highest current density (3.5 mA/cm^2 at 1.0 $V_{Ag/AgCl}$) was obtained on a 16.2% Ni-doped sample (green curve), instead of the highest concentration of Ni-doping at 30.9% (blue curve). Also, the onset of water oxidation for hematite samples doped with 16.2% and 30.9% Ni was similar, about 0.55 $V_{Ag/AgCl}$. This suggests that the top surface of the hematite nanoplates might be saturated with Ni after 16.2% Ni doping, since the onset potential is related to the chemical environment of the surface. As the concentration of Ni was further increased, Ni atoms diffused into the subsurface, leading to a more disordered lattice in the bulk, which is associated with a decrease in electron conductivity. This could explain why the current density for hematite samples with 30.9% Ni is lower than that with 16.2% Ni.

By comparing results from samples with different aspect ratios, the hematite nanosheet with the largest surface area ratio of the (0001) facet with respect to other facets exhibited the largest electrocatalytic activity enhancement in Fig. 9a. There is a 2.2 mA/cm^2 difference of current density at 1.0 $V_{Ag/AgCl}$ between un-doped and doped samples for water oxidation. As the (0001) facet area ratio decreases, the difference in current density decreases. To support these conclusions, we also performed electrochemical stability measurements of all samples with different morphologies and different levels of Ni-doping (Figure S5). There is no significant loss in electrocatalytic activity for all samples after 1 h. All of these results (i.e. reduction of onset potential and enhancement of current density) are consistent with both theoretical predictions[15] and previous fundamental studies[16] that Ni-incorporation into α-Fe_2O_3(0001) facilitates water oxidation.

Conclusions

HRTEM, SEM, XRD, Raman, BET, and XPS were used to characterize hematite and Ni-doped hematite nanoplates. We have demonstrated that we can continuously tune the aspect ratio and achieve fine control of the ratio of the exposed (0001) facet of hematite nanocrystals. The surface area ratio of the hexagonal (0001) surface can be tuned in a range from 98% to 30%. Ni doping is associated with diffusion of Ni into the subsurface region, forming a uniformly doped $Ni_xFe_{2-x}O_3$ surface overlayer that improves the electrocatalytic activity of water oxidation. Doped Ni atoms most likely occupy the lattice positions of Fe atoms rather than occupying interstitial positions. These results are discussed in the context of a theoretical prediction[15] and subsequent experimental validation[16] that Ni doping facilitates the water oxidation reaction on hematite (0001) surfaces. Electrochemical testing for the water oxidation reaction was also carried out on these hematite nanocrystals with different shapes. The enhancement of water oxidation activity by Ni-doping increases as the surface area ratio of the (0001) facet of hematite nanocrystals increases.

Acknowledgements

This work is supported by the National Science Foundation under Grant No. CHE-1465082.

References

1 K. Sivula, F. Le Formal and M. Gratzel, *ChemSusChem*, 2011, **4**, 432-449.
2 Y. J. Lin, G. B. Yuan, S. Sheehan, S. Zhou and D. W. Wang, *Energy Environ. Sci.*, 2011, **4**, 4862-4869.
3 N. T. Hahn, H. C. Ye, D. W. Flaherty, A. J. Bard and C. B. Mullins, *Acs Nano*, 2010, **4**, 1977-1986.

4 A. Kay, I. Cesar and M. Gratzel, *J. Am. Chem. Soc.*, 2006, **128**, 15714-15721.

5 L. Vayssieres, C. Sathe, S. M. Butorin, D. K. Shuh, J. Nordgren and J. H. Guo, *Adv Mater*, 2005, **17**, 2320-+.

6 X. D. Li, Z. Wang, Z. M. Zhang, L. L. Chen, J. L. Cheng, W. Ni, B. Wang and E. Q. Xie, *Sci Rep-Uk*, 2015, **5**.

7 S. D. Tilley, M. Cornuz, K. Sivula and M. Gratzel, *Angew Chem Int Edit*, 2010, **49**, 6405-6408.

8 P. Zhao, C. X. Kronawitter, X. F. Yang, J. Fu and B. E. Koel, *Phys. Chem. Chem. Phys.*, 2014, **16**, 1327-1332.

9 F. K. Meng, J. T. Li, S. K. Cushing, J. Bright, M. J. Zhi, J. D. Rowley, Z. L. Hong, A. Manivannan, A. D. Bristow and N. Q. Wu, *Acs Catal*, 2013, **3**, 746-751.

10 M. W. Louie and A. T. Bell, *J. Am. Chem. Soc.*, 2013, **135**, 12329-12337.

11 S. H. Shen, C. X. Kronawitter, D. A. Wheeler, P. H. Guo, S. A. Lindley, J. G. Jiang, J. Z. Zhang, L. J. Guo and S. S. Mao, *J Mater Chem A*, 2013, **1**, 14498-14506.

12 Y. Liu, Y. X. Yu and W. D. Zhang, *Electrochim. Acta*, 2012, **59**, 121-127.

13 W. R. Cheng, J. F. He, Z. H. Sun, Y. H. Peng, T. Yao, Q. H. Liu, Y. Jiang, F. C. Hu, Z. Xie, B. He and S. Q. Wei, *J. Phys. Chem. C*, 2012, **116**, 24060-24067.

14 Y. S. Hu, A. Kleiman-Shwarsctein, A. J. Forman, D. Hazen, J. N. Park and E. W. McFarland, *Chem. Mater.*, 2008, **20**, 3803-3805.

15 P. L. Liao, J. A. Keith and E. A. Carter, *J. Am. Chem. Soc.*, 2012, **134**, 13296-13309.

16 P. Zhao and B. E. Koel, *Acs Appl Mater Inter*, 2014, **6**, 22289-22296.

17 Y. Yang, H. X. Ma, J. Zhuang and X. Wang, *Inorg Chem*, 2011, **50**, 10143-10151.

18 T. K. Townsend, E. M. Sabio, N. D. Browning and F. E. Osterloh, *Energy Environ. Sci.*, 2011, **4**, 4270-4275.

19 L. Q. Chen, X. F. Yang, J. A. Chen, J. Liu, H. Wu, H. Q. Zhan, C. L. Liang and M. M. Wu, *Inorg Chem*, 2010, **49**, 8411-8420.

20 X. L. Hu and J. C. Yu, *Adv Funct Mater*, 2008, **18**, 880-887.

21 F. Q. Lu, Q. L. Wu, X. F. Yang, L. Q. Chen, J. J. Cai, C. L. Liang, M. M. Wu and P. K. Shen, *Phys. Chem. Chem. Phys.*, 2013, **15**, 9768-9774.

22 M. R. Waller, T. K. Townsend, J. Zhao, E. M. Sabio, R. L. Chamousis, N. D. Browning and F. E. Osterloh, *Chem. Mater.*, 2012, **24**, 698-704.

23 P. Zhao, D. S. Wang, J. Lu, C. Y. Nan, X. L. Xiao and Y. D. Li, *J Mater Res*, 2011, **26**, 424-429.

24 Y. E. Wu, D. S. Wang, P. Zhao, Z. Q. Niu, Q. Peng and Y. D. Li, *Inorg Chem*, 2011, **50**, 2046-2048.

25 D. S. Wang, P. Zhao and Y. D. Li, *Sci Rep-Uk*, 2011, **1**.

26 D. S. Wang, Z. Y. Wang, P. Zhao, W. Zheng, Q. Peng, L. Q. Liu, X. Y. Chen and Y. D. Li, *Chem-Asian J*, 2010, **5**, 925-931.

27 S. Brunauer, P. H. Emmett and E. Teller, *J. Am. Chem. Soc.*, 1938, **60**, 309-319.

28 D. Bersani, P. P. Lottici and A. Montenero, *J Raman Spectrosc*, 1999, **30**, 355-360.

29 X. B. Chen, L. Liu, P. Y. Yu and S. S. Mao, *Science*, 2011, **331**, 746-750.